Quad-Furcated Profiled Horn: The Next Generation Highly Efficient GEO Antenna in Additive Manufacturing

Charalampos Stoumpos, Jean-Philippe Fraysse, George Goussetis, Ronan Sauleau, Hervé Legay

This article has been accepted for publication in a future issue of this journal, but has not been fully edited. Content may change prior to final publication. Citation information: DOI 10.1109/OJAP.2021.3134833, IEEE Open Journal of Antennas and Propagation

Quad-Furcated Profiled Horn: The Next Generation Highly Efficient GEO Antenna in Additive Manufacturing

Charalampos Stoumpos, Jean-Philippe Fraysse, George Goussetis, *Senior Member, IEEE*, Ronan Sauleau, *Fellow, IEEE* and Hervé Legay

Abstract—A novel compact and highly efficient dual-polarized horn-like antenna is presented. It exploits a radiating aperture that is fed by four smaller waveguides via a quad-furcated junction. The antenna also comprises the full feed network for the feed waveguides including an integrated 4-way orthomode power divider. Design principles are described in detail and illustrated by means of an example involving an antenna with aperture size of $2.6\lambda_0 \times 2.6\lambda_0$ (λ_0 the wavelength at the central frequency of operation) intended primarily for Geostationary Orbit (GEO) satellites. The antenna feed was designed to comply with the Additive Manufacturing rules and exhibits aperture efficiency levels close to the theoretical maximum ones over the entire transmit Ku band (10.7 – 12.75 GHz), while at the same time its profile is highly compact ($6.4\lambda_0$). The measured results of a prototype 3D-printed in Selective Laser Melting (SLM) verified experimentally the calculated high aperture efficiency (over 90%). The total antenna feed attains return loss > 19 dB and maximum cross-polarization isolation (XPI) > 24 dB over a bandwidth of 18%. In light of the favorable electrical performances and compact size, the proposed solution constitutes an appealing alternative to profiled (or spline) horns for satellite antenna systems used either as reflector feeds or direct radiating arrays.

***Index Terms*—Additive manufacturing, aperture antenna, aperture efficiency, dual-polarization, excitation network, four-way orthomode power division, GEO antenna, quad-furcated radiating element, satellite feeds.**

I. Introduction

Horn Antennas are widely used in various microwave and millimeter-wave applications. In satellite missions, horn antennas are commonly deployed as feed elements for reflectors, in phased arrays, as well as in calibration and gain measurements [1]. Their wide range of applicability is attributed to their excellent RF performance such as high gain, broad bandwidth and very low losses. The advent of broadband connectivity via satellites is presently driving the development of high performance multibeam antenna architectures including direct radiating arrays (DRAs) or array fed reflectors (AFR) [2]. These applications typically call for dual-polarization, low cross-polarization, rotationally symmetric radiation patterns and high power-handling capability. Additional desirable features are high aperture efficiency, such that a given horn aperture can achieve increased gain [3], as well as reduced volume and mass that will simplify the on-board accommodation.

For aperture sizes up to $2\lambda_0$, many candidate antenna solutions with excellent RF performance and low profile have been developed. These solutions include the Scrimp horn [4, 5], the short backfire antenna [6-9] or the stacked Fabry-Perot cavity antenna [10]. However, for the aforementioned radiating elements, the bandwidth and the aperture efficiency decrease steadily as the radiating aperture is increased. For GEO satellite applications, typical aperture size requirements are in the range of $2.4\lambda_0 \sim 3.4\lambda_0$, for which the aforementioned antennas fail to achieve the required RF performance. Therefore, for radiating elements with apertures larger than $2\lambda_0$ and high aperture efficiency levels, antenna options include dielectric-filled [11, 12], lens-corrected [13], partly corrugated (hard) [14], metamaterial-based horns (metahorns) [15, 16] or spline profile multimode horns [17-26]. Dielectric-loaded and hard horns can reach efficiency levels close to the theoretical maximum at a cost of increased height and weight. Materials properties (especi-

Manuscript received October 22, 2021; This work was supported by the European Union's Horizon 2020 research and innovation program under the Marie Skłodowska-Curie Grant Agreement REVOLVE No. 722840.

C. Stoumpos was with the School of Engineering and Physical Sciences, Heriot-Watt University, Edinburgh EH14 4AS, U.K. and now is with the Univ Rennes, CNRS, Institut d'Electronique et des Technologies du numéRique (IETR) — UMR CNRS 6164, F-35000 Rennes, France and also with the Research and Development Department, Thales Alenia Space, 31037 Toulouse, France (e-mails: Charalampos.Stoumpos@insa-rennes.fr, haris_stou@hotmail.com).

J. P. Fraysse and H. Legay are with the Research and Development Department, Thales Alenia Space, 31037 Toulouse, France. (e-mail: {jean-philippe.fraysse; herve.legay}@thalesaleniaspace.com).

G. Goussetis is with the School of Engineering and Physical Sciences, Heriot-Watt University, Edinburgh EH14 4AS, U.K. (e-mail: g.goussetis@hw.ac.uk).

R. Sauleau is with the Univ Rennes, CNRS, Institut d'Electronique et des Technologies du numéRique (IETR) — UMR CNRS 6164, F-35000 Rennes, France (e-mail: ronan.sauleau@univ-rennes1.fr).

Digital Object Identifier xxx/OJAP.202x.xxx

This article has been accepted for publication in a future issue of this journal, but has not been fully edited. Content may change prior to final publication. Citation information: DOI 10.1109/OJAP.2021.3134833, IEEE Open Journal of Antennas and Propagation

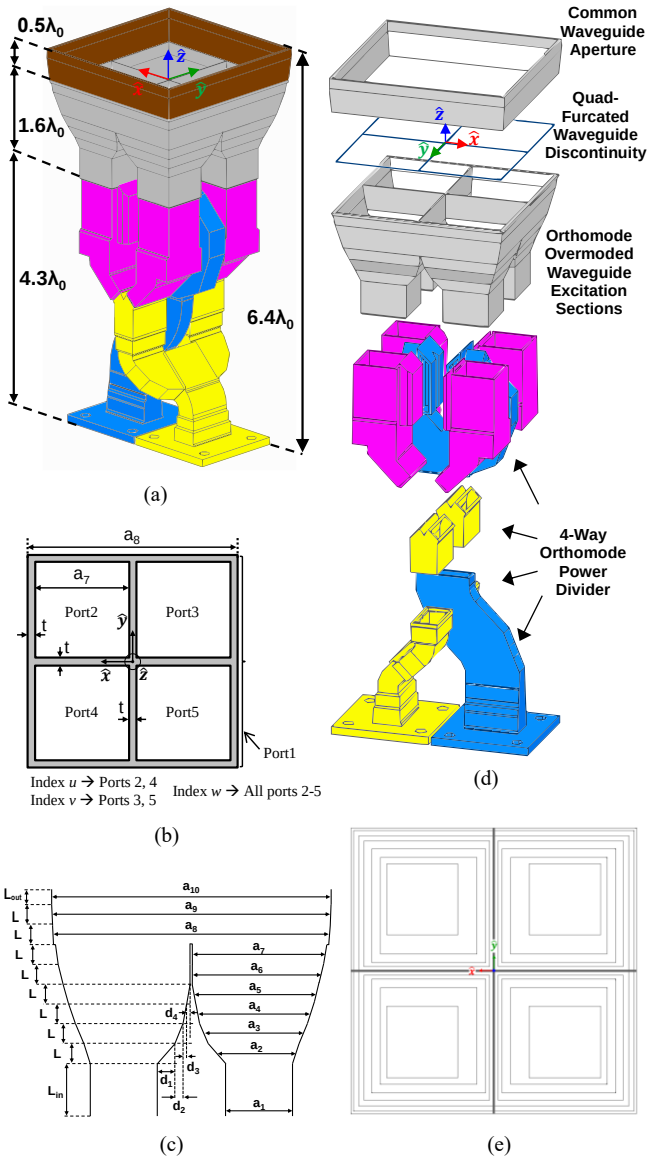

Fig. 1. Configuration and geometry of the proposed full-corporate dual linearly polarized square Quad-Furcated Profiled Horn Antenna (Q-FPHA) feed (input port 1 in yellow and input port 2 in blue): (a) the total antenna, (b) geometry of the 4-furcated waveguide surface discontinuity, (c) side cut-view with dimensional variables of the 4-port radiating element, (d) exploded view of the total antenna and (e) top view of the 4-port radiating element.

ally outgassing) as well as requirements for supplementary treatment linked with electrostatic discharge (ESD) effects prevent their use when it comes to spaceborne applications.

Consequently, current practice relies on the use of spline profile multimode horns. As dictated by aperture theory [1, 18], high levels of aperture efficiency are associated with a given distribution of modes on the radiating aperture of a horn. Spline horns achieve this modal distribution by virtue of modulating their cross-section along an elongated flaring section [18]. In spite of their advantageous characteristics, spline horns present two basic drawbacks. On one hand, the product of aperture efficiency with the bandwidth is capped. According to the state-of-the-art design principles [18], square spline-profile horns with aperture sizes around $3\lambda_0 \times 3\lambda_0$ present high aperture efficiencies (close to 90%) for a fractional frequency bandwidth around 10%. On the other hand, the longitudinal profile of spline horns is typically high; for aperture sizes around $3\lambda_0 \times 3\lambda_0$ the profile can vary in the range $6.5\lambda_0$ to $10\lambda_0$ in order to achieve aforementioned levels of aperture efficiency. For design examples based on advanced optimization techniques demonstrate aperture efficiency in the range between 85%~90% for a wider bandwidth (around 20%) at a cost of a significantly larger profile ($\approx 10\lambda_0$) [19]. It is noted that since these radiating elements require an external OMT the final axial profile of a total antenna feed system which will comprise both modules (OMT and spline horn), typically exceeds levels of $10\lambda_0$.

Several researches have targeted to address the limitation of spline horns. In [20], compact [without the inclusion of the orthomode transducer (OMT)] and highly efficient but with a moderate bandwidth (10%) spline multimode circular aperture horns for aperture radii varying from $2\lambda_0$~$6\lambda_0$ have been presented. A similar process has been followed in [21]. In [22], a dual-band circular aperture horn with aperture efficiency levels over 80% (for both bands) has been published. A design methodology and the characterization of compact highly efficient horn antennas in single polarization and aperture sizes varying from $1.25\lambda_0$~$3\lambda_0$ has been presented in [23], while in [24] a very efficient dual-band spline profiled horn in dual polarization has been demonstrated. Flight qualified spline square horns with an aperture size of $2.6\lambda_0 \times 2.6\lambda_0$ and a more compact profile ($5\lambda_0$) have been presented in [25, 26], but they suffer from reduced aperture efficiency (80%-85%) across the frequency bandwidth of the Ku-Tx band. In [27], subarrays of spline horns with dedicated beam forming networks have been presented; an aperture efficiency level of the order of 85~88% has been characterized, while the profile of only the subarrays is rather compact (4.4 λ_0) however for a narrow bandwidth (2.5%).

In this paper, we present the Quad-Furcated Profiled Horn Antenna (Q-FPHA) which is a new approach to address the requirement for simultaneously highly efficient, broadband and compact horns. The concept is illustrated in Fig. 1 and as shown, the antenna feed integrates a 4-way dual polarized orthomode waveguide power divider feeding an array of four asymmetrically flared orthomode and overmoded waveguide sections. These in turn excite a 4-furcated waveguide surface discontinuity which is connected to a common square waveguide leading to the radiating aperture. An initial approximation of the design concept was first implemented in a single-polarized bi-furcated H-plane horn antenna [28]. After experimentally verifying the high levels of aperture efficiency, the more demanding in terms of complexity but more important in terms of practical needs Q-FPHA was further studied and developed. The proposed solution (but not the design procedure and the experimental verification, which are original contributions of this paper) has been filed by Thales Alenia Space [29]. For a visually similar (multi-access) but conceptually and operationally different horn antenna, 97% aperture efficiency is also reported without any

bandwidth indication [30]; experimental demonstrations are also yet needed to prove this claim. In a different framework (monopulse horn design) and with a more reduced bandwidth, the idea of feeding the aperture with 4 different waveguides with the objective of generating different patterns (sum and difference) has been addressed [31].

The proposed radiating element manages to achieve a modal distribution close to the ideal one over a large frequency bandwidth, while at the same time presents a relatively compact profile including the feeding network. To the authors' best of knowledge, this is the first square aperture, dual-polarized, purely-metallic, full-corporate (OMT included) horn antenna that can achieve aperture efficiency values close to the theoretical maximum over a frequency bandwidth larger than 15% and for aperture sizes above $2\lambda_0$, while maintaining an axial profile lower than $6.5\lambda_0$. The aperture efficiency was verified experimentally after the measurements of a 3D-printed in SLM prototype without any further surface treatment or metallization (i.e. silver plating) process. The compact design, broadband performance, high aperture efficiency, high isolation, low cross-polarization as well as low multipaction and passive intermodulation (PIM) performance make the Q-FPHA an ideal solution for GEO spaceborne applications.

II. High Aperture Efficiency Principles

An ideal radiating aperture that achieves aperture efficiency of 100% is excited with a uniform radiating field in amplitude and phase. For a horn antenna, the radiated field can be decomposed as a superposition of propagating waveguide modes associated with the transverse section of its aperture [32]-[34]. The size of the aperture will then define which modes are propagating and hence contributing to the radiation. Design guidelines for high aperture efficiency stepped horn have been presented by *Bhattacharyya et al.*, proving that for a dual-polarized rectangular or square) aperture, the optimal distribution is the one that dictates the excitation of the aperture modes TE_{m0}, m=1, 3, 5, … in equal phase and amplitude of the order of $1/m$ [18]. As later shown by *Bird et al.*, this is close to optimum (tends asymptotically to 100% as $m\rightarrow\infty$) when mismatch and mode coupling at the aperture is small [2], [23]. This is the case for electrically moderate and large apertures (i.e. typically above $2\lambda_0\times2\lambda_0$), where the maximum efficiency for a rectangular (or square) horn with TE_{m0} m=1, 3, 5, …, M, being the highest propagating mode at the aperture is defined by the following formula [2]:

$$\eta_{\max}=\frac{8}{\pi^2}\sum_{m=1,\,3,\,5,\,\ldots}^{M}\left(\frac{1}{m^2}\right) \tag{1}$$

It is appreciated that the size of the aperture will define which modes are propagating and hence contributing to the radiation. This in turn will define the maximum efficiency that can be achieved according to the truncation of the series in eq. (1), which is achieved when a total field of unitary power is distributed to the three identified modes with equal phase and amplitude as:

$$[F]=\begin{bmatrix}F_{h_{10}}\\F_{h_{30}}\\F_{h_{50}}\end{bmatrix}\approx\begin{bmatrix}0.932\\0.3107\\0.1864\end{bmatrix} \tag{2}$$

where $[F]$ is a vector with the aperture modal content, while $F_{h_{m0}}$ are the individual modal amplitudes of the modes TE_{m0}, m=1, 3, 5 for the case of an aperture size of $2.6\lambda_0\times2.6\lambda_0$.

For spline horns, this modal distribution is achieved by optimizing their profile, where appropriate discontinuities control the aperture modal content. In this work, we exploit the structure illustrated in Fig. 1, the design of which is described in section III by means of a design example.

III. Design Principles

The selected frequency band of operation for the proposed radiating element is the Ku-Tx band (10.7 – 12.75 GHz). This band is commonly used for multiple beam applications (MBA) for global coverage [3] and the antenna specifications are provided in Table I. These specifications are typical for the targeted missions [25, 26]. Square apertures are preferred to circular ones such that full utilization of the available space on the satellite will be made when the radiating elements will be arrayed (packaging efficiency). Only square and hexagonal apertures offer 100% array packaging efficiency, while circular aperture is reduced to 90%. From scanning requirement point of view, however, circular elements in hexagonal grid are preferable because about 13% lesser elements are required. The aperture size is $2.6\lambda_0\times2.6\lambda_0$ is typical of horns employed in GEO satellite applications. For a maximum scanning angle (coverage region) of 8.7˚, in an array configuration this inter-element distance produces grating lobes outside this coverage/scan angle (closest grating lobe at 13.5˚) [35].

A. Outline of the Design Methodology

The design methodology of the presented type of radiating element commences with the ideal modal distribution given in eq. (2). The process exploits two stages. With reference to Fig. 1, the first stage targets to achieve the required power

TABLE I
Specifications of Antenna Feeds for GEO MBA in Ku-Band

Antenna Aperture	Square $2.6\lambda_0\times2.6\lambda_0$
Frequency Band	Ku-Tx (f_0= 11.725 GHz)
Fractional Bandwidth	> 18%
Technology	Waveguide (Purely Metallic)
Profile (Including OMT)	Compact (< $7\lambda_0$)
Polarization	Dual-Linear
Return Loss	> 21 dB
Isolation	> 50 dB
Aperture Efficiency	> 90%
Cross-Polarization Isolation (XPI)	> 30 dB (over 10° solid angle) > 25 dB (over 20° solid angle)

This article has been accepted for publication in a future issue of this journal, but has not been fully edited. Content may change prior to final publication. Citation information: DOI 10.1109/OJAP.2021.3134833, IEEE Open Journal of Antennas and Propagation

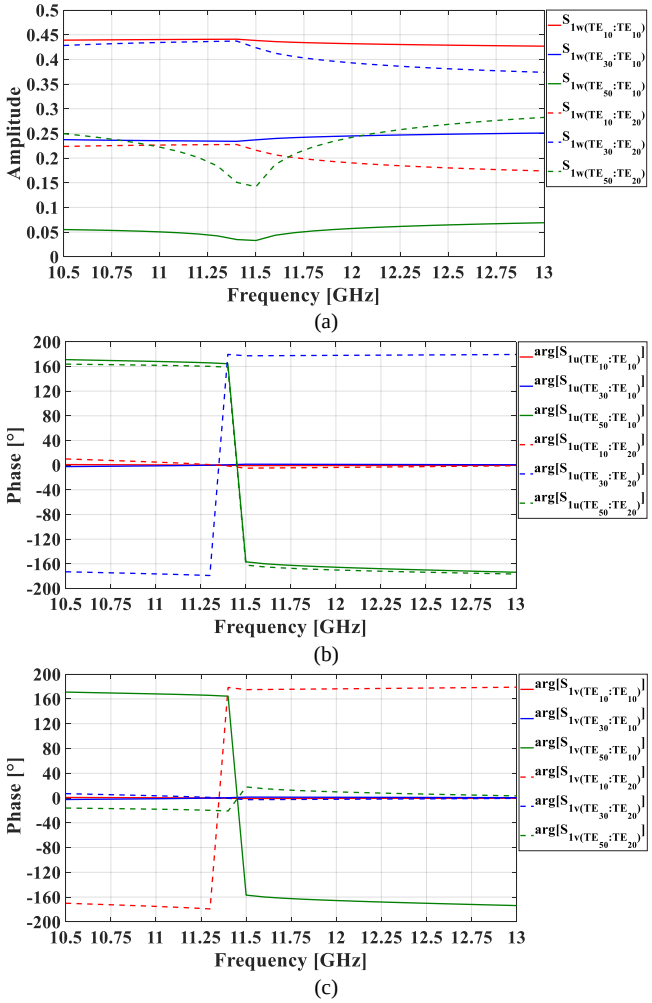

Fig. 2. Modal transmission coefficients among the modes TE_{10}, TE_{20} of the four (u = 2, 4 & v = 3, 5) excitation waveguides and the modes TE_{10}, TE_{30} and TE_{50} of the common (port 1) waveguide for the 4-furcated waveguide surface discontinuity. (a) Amplitude. (b) Phase for the input waveguides u = 2, 4. (c) Phase for the input waveguides v = 3, 5.

distribution across the three modes at the interface of the quad-furcated discontinuity with the common waveguide apertures as per eq. (2). The phase alignment is then achieved in a second phase and on the basis of the following observations. Firstly, the common aperture does not modify the power distribution on the propagating modes. Secondly, every mode presents a distinct propagation constant associated with the order mode [32]. Thus, the phases of the aperture modes can be adjusted at a second design stage with a low optimization complexity. Consequently, the emphasis is placed on the first stage of the design process, which focuses on the quad-furcated discontinuity and the modal distribution of the four feeding orthomode waveguides. In the remaining we thus focus on the excitation network and up to the quad-furcated discontinuity.

B. The 4-furcated Waveguide Surface Discontinuity

The quad-furcated surface discontinuity is the interface between the four excitation waveguides and the common waveguide leading to the radiating aperture. The geometry of a symmetrical quad-furcation is defined in Fig. 1(b). At this interface, the modes of the radiating aperture are excited in appropriate weights. The transmission coefficients between the common square waveguide and each of the four excitations thus define the targeted complex (magnitude and phase) modal content delivered by the excitation waveguides. On this basis, the other design constraint is that the incoming modes from the excitation waveguides are well matched at this interface. The Mode-Matching method [36, 37] is a convenient technique for the study of this discontinuity. This technique allows extracting the Generalized Scattering Matrix (GSM). In the remaining we use the notation F_w^{il} and B_w^{il} for the forward and backward modal voltages in the excitation waveguides, while F_1^{mn} and B_1^{mn} for the forward and backward modal voltage at the common port of the quad-furcation.

Next, we proceed with the investigation of the modal coupling coefficients at the quad-furcation. In light of the requirement for dual-polarized operation, we are considering a discontinuity with symmetry along the x- and y-axes. With reference to Fig. 1(b), the geometry is thus defined by the dimensions of the square excitation waveguides (a_7) and the common waveguide (a_8) as well as the gap between each pair of them as well as the boundary of the common waveguide [$t=(a_8-2a_7)/3$]. On this basis, the magnitude of scattering parameters between port 1 and all other ports is identical for same or mirror symmetric excitation waveguides. The corresponding phases will thus be identical for the waveguides 2, 3 and 4, 5 considering polarization in x-axis and for the waveguides 2, 4 and 3, 5 for polarization in y-axis. Without loss of generality, for the analysis in the remaining of this paper the reference polarization is considered along y-axis.

For this analysis we consider the common waveguide aperture edge to be a_8=65.4mm. This is approximately equal to $2.55\lambda_0$, such that it reaches $2.6\lambda_0$ at the radiating aperture after some flaring. The edge of the excitation waveguides is considered a_7=32.1mm (approximately $1.25\lambda_0$). This was selected following a parametric study (not shown for brevity), which indicated that smaller waveguides lead to increased reflection of the TE_{20} mode associated with its frequency cutoff region.

Fig. 2(a) shows the amplitudes of the transmission coefficients between the TE_{10}, TE_{20} modes of the excitation waveguides (ports 2-5) and the modes TE_{10}, TE_{30} and TE_{50} of the common waveguide (port 1). The dominant TE_{10} mode from the excitation waveguides couples to the dominant TE_{10} mode of the common aperture [$S^c_{1w(h_{10}:h_{10})}$, solid red line] at normalized levels of about 0.45, while to the mode TE_{30} of the common aperture [$S^c_{1w(h_{30}:h_{10})}$, solid blue line] at normalized levels of about 0.25. It is noted that this ratio is higher than what is prescribed by eq. (2). The corresponding phases are plotted in Fig. 2(b) for the excitation waveguide pair with index u (ports 2, 4) and Fig. 2(c) for the excitation waveguide pair with index v (ports 3, 5).

This article has been accepted for publication in a future issue of this journal, but has not been fully edited. Content may change prior to final publication. Citation information: DOI 10.1109/OJAP.2021.3134833, IEEE Open Journal of Antennas and Propagation

Next, assuming that the two waveguide excitation modes are the TE_{10} and TE_{20} (F_w^{il}, i=1, 2 and l=0), while the rest are zero and suppressing the common waveguide modal reflection coefficient matrix $[S_{11pp}^c]$ as it contributes to the power normalization of each mode at the common waveguide ($F_1^{h_m0}$, m = 1, 3, 5), the non-normalized modal vector is written as:

$$\begin{bmatrix} F_1^{h_{10}} \\ F_1^{h_{30}} \\ F_1^{h_{50}} \end{bmatrix} = \frac{1}{2} \begin{bmatrix} \sum_{w=2}^{5} \left(F_w^{h_{10}} \cdot S_{1w(h_{10}:h_{10})} + F_w^{h_{20}} \cdot S_{1w(h_{10}:h_{20})} \right) \\ \sum_{w=2}^{5} \left(F_w^{h_{10}} \cdot S_{1w(h_{30}:h_{10})} + F_w^{h_{20}} \cdot S_{1w(h_{30}:h_{20})} \right) \\ \sum_{w=2}^{5} \left(F_w^{h_{10}} \cdot S_{1w(h_{50}:h_{10})} + F_w^{h_{20}} \cdot S_{1w(h_{50}:h_{20})} \right) \end{bmatrix} \quad (3)$$

The factor 1/2 at the beginning assures that the total power of the 5-port network is normalized to 1. It has been considered that the amplitude of the input modes to the 4-furcated waveguide surface discontinuity is identical for the four input waveguide sections.

Eq. (3) is the approximated and simplified form of the quad-furcated surface waveguide discontinuity's coupling matrix. Referring to Fig. 1(b), only the modal transmission coefficients between the common waveguide's (port 1) propagating modes TE_{10}, TE_{30}, TE_{50} and the four excitation waveguides' propagating modes TE_{10}, TE_{20} have been taken into account. From Figs. 2(b) and 2(c), five significant conditions are derived and summarized in the Appendix [eqs. (A1) - (A5)].

In addition, it is observed that if $|h_{20}^{\text{in}}| \neq 0$, $|S_{1w,h_{m0} \to h_{20}}^c| \neq 0$, m=1, 3, 5, each second term of every summation in eq. (3) will be suppressed and there will no longer be a contribution from the mode TE_{20}, if and only if $\varphi_{w,h_{20}}$ is the same $\forall$ w=2, 3, 4, 5 due to eq. (A3). In this context, the excitation waveguides should be designed according to the following relation:

$$\left| \varphi_{u,h_{20}^{\text{in}}} - \varphi_{v,h_{20}^{\text{in}}} \right| = 180^\circ \Rightarrow e^{j\varphi_{u,h_{20}^{\text{in}}}} = -e^{j\varphi_{v,h_{20}^{\text{in}}}},\ u=2,\ 4\ \&\ v=3,\ 5 \quad (4)$$

The last issue to be investigated relates to the coupling between the excitation modes (h_{10}^{in} and h_{20}^{in}) and the rest undesired propagating higher order modes on the common aperture; the TE higher order modes of the form of $F_1^{h_{mn}}$, n≠0, as well as all the TM modes. These modes can be separated into two categories. The first one relates to the common aperture propagating modes in the form of TE_{mn}, TM_{mn}, m=2k, n=2k-1, k ∈ N* (TE_{12}, TM_{12}, TE_{14}, TM_{14}, TE_{32}, TM_{32}, TE_{34}, TM_{34}, TE_{52} and TM_{52}), as well as the modes TE_{mn}, m=0, n=k, k ∈ N*. The coupling between the excitation modes (h_{10}^{in} and h_{20}^{in}) and this first family of higher order modes is negligible and presents modal transmission coefficient amplitudes below -40 dB. The second category refers essentially to all rest modes excluding the desired aperture modes and those of the first family. These modes do couple with the excitation modes (h_{10}^{in} and h_{20}^{in}) but by virtue of operation [eq. (4)] they add up 180° out of phase from the excitation waveguides and so they are canceled out from the common output waveguide region.

C. Design Methodology of the 4 Input Square Waveguides

The design methodology of the four excitation waveguide parts is driven by the condition posed from eq. (4) which arose from the propriety of the 4-furcated discontinuity's propriety expressed in eq. (A3). Moreover, keeping in mind that the proposed radiating element is a dual-polarized antenna, this feature should be valid for both polarizations at the transversal $\hat{\mathbf{x}}\hat{\mathbf{y}}$ plane [Fig. 1(b)]. Besides, a third obvious prerequisite is that each of the four input waveguides should end up to overmoded output square waveguides, so that they can generate a certain level of the required TE_{20} mode.

The three aforementioned points are satisfied by the four conceived excitation waveguides [the section from a1 to a7 depicted in Fig. 1(c)]. The first feature of this tapered waveguide section is its lateral displacements to each (or potentially some) waveguide section for the generation of the TE_{20} mode. This means that in order to generate the mode TE_{20}, some waveguides from the tapered profile of the total feed waveguide section have been displaced laterally. Moreover, in contrast to the simpler bi-furcated case [28], every adjacent feed waveguide section is symmetric with respect to both $\hat{\boldsymbol{x}}\hat{\boldsymbol{z}}$ and $\hat{\boldsymbol{y}}\hat{\boldsymbol{z}}$ planes with reference to Figs. 1(b) and 1(e), resulting in a mirror symmetric array of the four feed waveguide sections. On one hand, this feature enables the four waveguides to generate the mode TE_{20} 180° out of phase between the waveguide pairs u and v as prescribed in eq. (4). On the other hand, the dual-polarization is assured. This feature constitutes the key effect of this concept as it results to the properly weighted excitation of the targeted modal content right after the quad-furcation (at its larger/common port). This is better illustrated by the algebraic manipulations (A6)-(A8) in the Appendix. Upon these considerations, the final system of equations [eq. (A8)] includes three equations with two unknown variables; the modal amplitude ratio $|h_{20}^{\text{in}}|/|h_{10}^{\text{in}}|$ [due to eq. (A9)] and the phase difference $\Delta\varphi_{\text{in}}$ of the excitation waveguides. These two quantities will occur from the design of the four input tapered waveguide parts which present an overmoded output. Therefore, eq. (A8) is an over-determined system and we are interested in solutions that induce the least inconsistency.

Thereinafter, the orthomode excitation waveguide section depicted in Fig. 1(c) was designed and optimized with the mode-matching technique across the frequency band of interest. Fig. 3 depicts the parametric analysis of the lateral waveguide displacements, where the progressive excitation of the mode TE_{20} can be identified. With reference to Fig. 1(c), the optimized geometrical parameters are as follows.

This article has been accepted for publication in a future issue of this journal, but has not been fully edited. Content may change prior to final publication. Citation information: DOI 10.1109/OJAP.2021.3134833, IEEE Open Journal of Antennas and Propagation

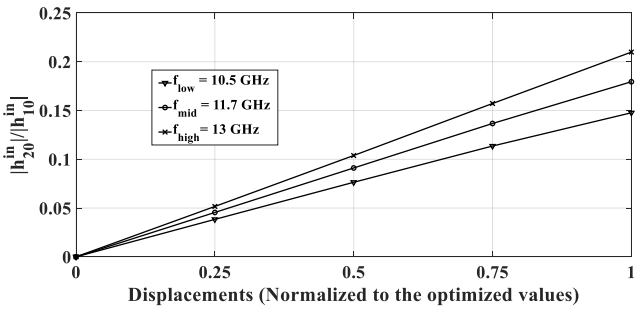

Fig. 3. Parametric analysis for the progressive excitation of the modal amplitude ratio $|h_{20}^{in}|/|h_{10}^{in}|$ on the output of each of the four excitation waveguide parts.

- a_i = {16.05, 21.8, 25.7, 28.3, 30.3, 31.5, 32.1} mm.
- d_i = {4.225, 1.95, 0.9, 0.8} mm.
- L_{in} = 20 mm and L = 4.75 mm.

Fig. 3 shows that the voltage amplitude ratio between h_{10}^{in} and h_{20}^{in} varies between 0.15 and 0.21. The amplitude of the rest higher order modes presents values below 0.18 (≈ -15 dB) and the reflection coefficient remains below 0.1 (-20 dB) across the total frequency bandwidth. The total profile of the waveguide structure excluding the input waveguide's length is about $1.1\lambda_0$. The length might be further reduced for a narrower frequency bandwidth.

A last point to be added is the case where the radiating element's aperture size is smaller than $2\lambda_0 \times 2\lambda_0$. In this case, the size of the four excitation waveguide sections would be smaller than $\lambda_0 \times \lambda_0$, resulting in the cut-off of the mode TE_{20}. This in turn means that eq. (3) will degenerate to a case where only the mode TE_{10} could be utilized. This fact sets a fundamental lower bound to the range of this method with respect to the aperture size of the radiating element. As a result, realistic implementations of this method relate to radiating elements that employ apertures with a size larger than at least $2.3\lambda_0 \times 2.3\lambda_0$.

D. Design of the 4-Port Radiating Element with a Common Waveguide Region

The last part for the finalization of the total 4-port radiating element's design relates to the inclusion of the top part. This is essentially the region where the correction of the output modal phase of the weighted modes that were formed right after the quad-furcated waveguide surface discontinuity will be attained. This upper part ends up to the final common radiating aperture of the total 4-port radiating element. Substantially, the phase of every propagating mode is dependent only by its propagation constant and its length [32], $\varphi_{F_1^{hm0}} = \gamma_{F_1^{hm0}} l$, where $\gamma_{F_1^{hm0}} = a_{F_1^{hm0}} + j\beta_{F_1^{hm0}}$, m = 1, 3, 5. For the lossless case, the modal phase is $\varphi_{F_1^{hm0}} = \beta_{F_1^{hm0}} l$, with $\beta_{F_1^{hm0}} = 2\pi/\lambda_{g_{F_1^{hm0}}}$ and $\lambda_{g_{F_1^{hm0}}}$ the phase constant and the guided wavelength of each propagating mode with the corresponding index m, respectively.

Finally, the upper common square waveguide section was designed with two slight supplementary discontinuities as it was observed that the phase of the mode TE_{50} can be adjusted better. With reference to Fig. 1(c), the optimized geometrical parameters of the common aperture are:

- a_8 = 65.4 mm, a_9 = 66.2 mm, a_{10} = 67 mm.
- L = 4.75 mm and L_{out} = 3.8 mm.

Fig. 4(a) shows the numerical results of the modal amplitude and Fig. 4(b) of the phase at the aperture, as well as the reflection coefficient at the input ports of the total 4-port radiating element represented as a 5-port network. For the calculation of the aperture modal content, the 4 orthomode ports have been excited simultaneously and the mode-matching technique was used to extract the radiating element's GSM. The results are identical for both polarizations (both degenerate input modes TE_{10} and TE_{01}) due to the transversal symmetry of the structure [Fig. 1(e)].

Fig. 4 indicates that the designed radiating element materializes with a very good agreement the ideal aperture modal voltage amplitude prescribed in eq. (2) for the frequency band of interest. The values of the aperture modal voltage amplitudes are defined at the quad-furcated surface discontinuity. The phase difference between the aperture modes is low; a maximum value of 80˚ is observed at the highest frequency (12.75 GHz) between TE_{30} and TE_{50}. This is because the design has been focused to deliver a better gain to the lower frequencies and therefore the upper common waveguide part has been adjusted to give the worst phase difference at the higher region of the frequency band. It is finally mentioned that the modal amplitude of the rest higher order modes maintains relatively low levels (below 0.13).

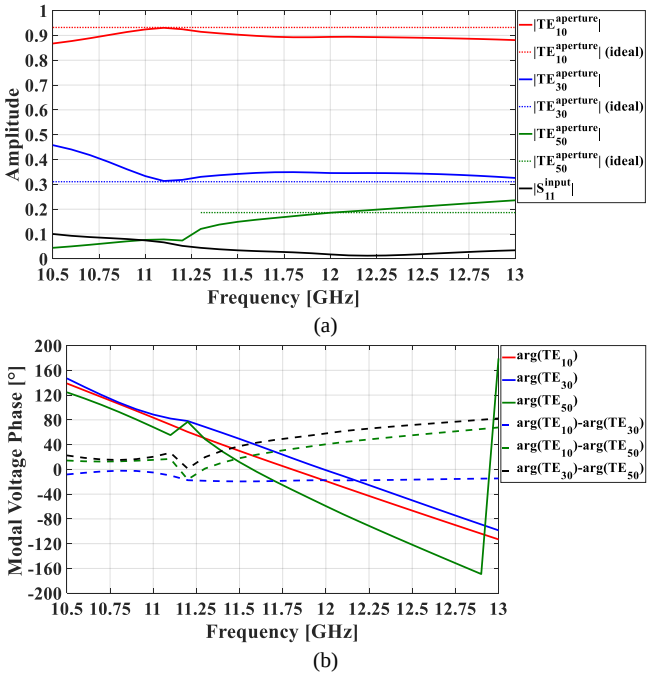

Fig. 4. The results of the optimized 4-port radiating element [Fig. 1(c)]: (a) aperture and ideal modal voltage amplitude of the modes TE_{10}, TE_{30}, TE_{50} and reflection coefficient at the input, (b) output modal phase of the modes TE_{10}, TE_{30}, TE_{50} and their relative phase difference.

This article has been accepted for publication in a future issue of this journal, but has not been fully edited. Content may change prior to final publication. Citation information: DOI 10.1109/OJAP.2021.3134833, IEEE Open Journal of Antennas and Propagation

E. The Excitation Network: Four-Way Dual-Polarized Waveguide Orthomode Power Divider

After the finalization of the 4-port radiating element, the last point for the development of the total antenna relates to its excitation. The requirement is a 4-way (2 single-mode WR75 input accesses × 4 dual-mode square output accesses) dual-polarized orthomode waveguide power divider. This device needs to provide the two orthogonal modes (TE_{10} and TE_{01}) in equal amplitude and phase at each of the 4-ports of the radiating element. It should also exhibit excellent RF performance for the minimization of the total antenna feed's losses as well as a compact profile.

Among several possible candidate solutions [38]-[52], in this work, a highly efficient 3D-printed 4-way orthomode waveguide power divider with equiamplitude and equiphasic power division scheme was selected to be used as an excitation network for the 4-port radiating element [53]. The general layout is illustrated in Figs. 1(a) and 1(d) (in yellow, blue and pink). This microwave device is a compact dual-polarized feeding network for antenna arrays and multiport radiating elements that exhibits low losses and is adapted to SLM. Its characterized dissipated losses present values below 0.1 dB for both routed channels (the two required orthogonal polarized components in a 4-way scheme), while its profile is $4.3\lambda_0$ [Fig. 1(a)]. Operational principles and experimental results can be found in [53]. It is worth mentioning that initial trials for the development of compact and highly efficient GEO antenna feeds involved much more compact feeder solutions [38], [39], [52]. However, various drawbacks of these candidates such as limited bandwidth [38], as well as mass, cost, complexity and additional losses [39], [52] led this research to employ more advanced manufacturing techniques for the development of such microwave networks.

IV. Experimental Results

Fig. 5 depicts the measurement setup [Figs. 5(a) and 5(b)] and the prototype [Fig. 5(c)] of the total additively manufactured dual-polarized square aperture Q-FPHA. The precision of the SLM process and hence the manufacturing tolerances are of the order of ±50μm. The 3D-printed prototype has not been subjected to further treatment (i.e. surface finishing) or metallization (i.e. silver plating). Finer lattice structures can be found at some parts of the antenna, while a less dense lattice was designed at the upper part. These were added for the enhancement of the mechanical stability during the printing process. The thickness of the waveguide walls is 1 mm and the body of the antenna was produced monolithically by a laser fiber that solidifies layer-by-layer the aluminum powder (AlSi10Mg). The printer that was used is the DMP Flex 350 from 3D systems. The antenna design is self-supported while few supplementary metallic parts were employed. On one hand, this prevents the increase of the total mass, while on the other hand no further milling is required to remove multiple additional supporting parts.

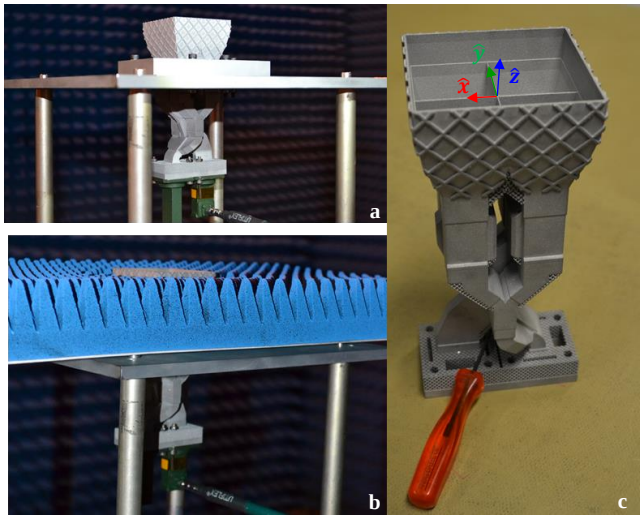

Fig. 5. Prototyping and measurement setup: a) AUT mounted on a metallic plate, b) final setup with the absorber below the AUT and c) prototype of the AM dual-polarized square aperture Q-FPHA (see Fig. 1 for axes orientation).

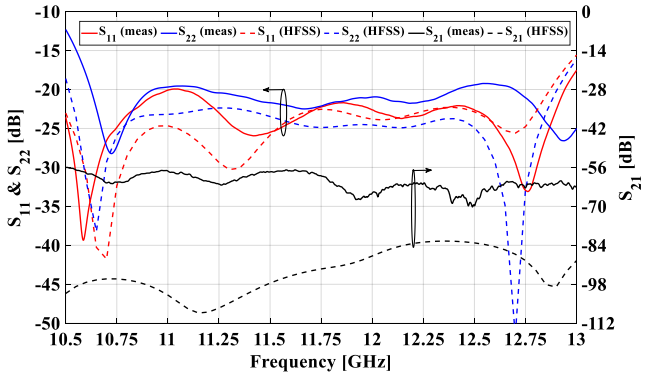

Fig. 6. Measured (solid lines) and simulated (dashed lines) reflection coefficients and coupling for the two input ports of the antenna.

In order to validate the radiation performance of the additively manufactured dual-polarized square aperture Q-FPHA, measurements in anechoic environment were performed. The antenna under test (AUT) was mounted on a metallic plate where it was centred and clamped with two extra metallic pieces [Fig. 5(a)]. Finally, an absorber was inserted so that the effect of the metallic plate lying below could be eliminated [Fig. 5(b)].

Fig. 6 depicts the measured and simulated S-parameters of the AM dual-polarized square aperture Q-FPHA. A close agreement between numerical and experimental results is observed. The measured reflection coefficients and particularly S_{22} exhibits a worst case of -19 dB at some frequencies within the Ku-Tx band. The slight deviations are attributed to the standard mechanical tolerances of the printing process. The port-to-port isolation is above 56 dB, a value that denotes an excellent decoupling between the two input ports.

Fig. 7 depicts the measured and numerically predicted broadside directivity across the frequency range of interest (10.5-13 GHz). Slight deviations (maximum of ±0.15 dB) owing to the manufacturing tolerances as well as the

This article has been accepted for publication in a future issue of this journal, but has not been fully edited. Content may change prior to final publication. Citation information: DOI 10.1109/OJAP.2021.3134833, IEEE Open Journal of Antennas and Propagation

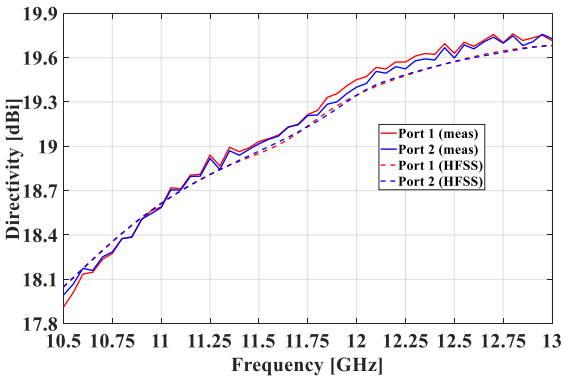

Fig. 7. Measured (solid lines) and simulated (dashed lines) broadside directivity across frequency for excitation of each input port.

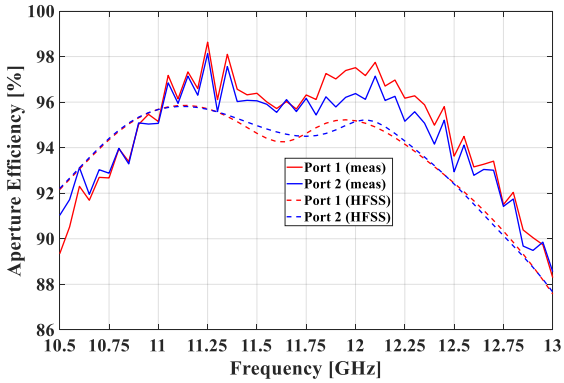

Fig. 8. Measured (solid lines) and simulated (dashed lines) aperture efficiency of the AM dual-polarized square aperture Q-FPHA.

uncertainty of the simulation tools and the measurement system are observed. The directivity values correspond to aperture efficiency levels above 92% for the 10.7-12.75 GHz band (Fig. 8). The aperture efficiency is defined as:

$$n_{\text{Ap.Eff.}} = \frac{\lambda^2 D_0}{4\pi A} \tag{5}$$

where λ the wavelength, D_0 the broadside directivity and A = 0.067×0.067 m^2, the aperture area of the antenna. In A, the aperture's flange thickness has not been taken into account. This thickness, by simulations has been evaluated to increase the directivity by 0.1~0.14 dB (depending on the frequency) which is translated to 2~3% (average of 2.5%) of aperture efficiency increase. Eq. (1) gives the theoretically maximum achievable aperture efficiency when mismatch and mode coupling at the aperture is small; a fact that occurs in electrically moderate or large apertures. Therefore, eq. (1) denotes that when m = 1, 3, 5, which corresponds to our case, this upper bound is 93.3%.

To further illustrate and better understand the radiation performance of the AM dual-polarized square aperture Q-FPHA, Figs. 9(a)-(d) show the measured normalized far-field directivity pattern of the AM antenna feed at the central operational frequency of 11.7 GHz (dashed lines). The co-polarized pattern is shown for the case of the three principal cuts [φ = 0˚, 45˚, 90˚ in Figs. 9(a)-(c), respectively] and the cross-polarized pattern at the D-plane case [φ = 45˚ in Fig.

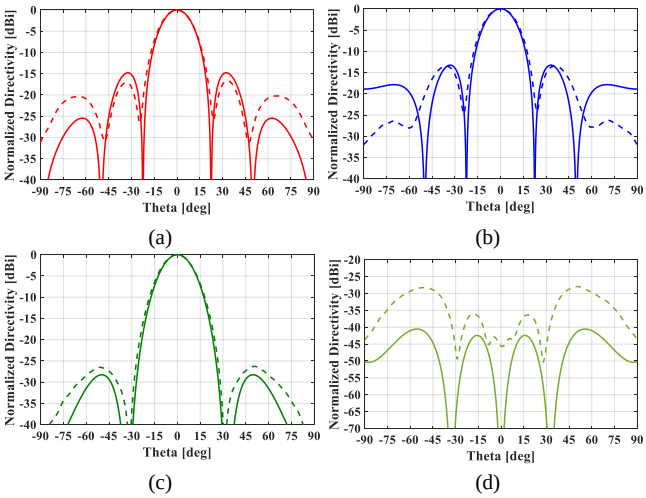

Fig. 9. Normalized measured radiation pattern at the central frequency f_0=11.7 GHz and comparison with the ideal case of a 2.6λ_0 × 2.6λ_0 aperture with a uniform e-field distribution: (a) co-polar e-plane cut, (b) co-polar h-plane cut, (c) co-polar d-plane cut, (d) cross-polar d-plane cut. Solid line: ideal (100% aperture efficiency) case. Dashed line: measured results.

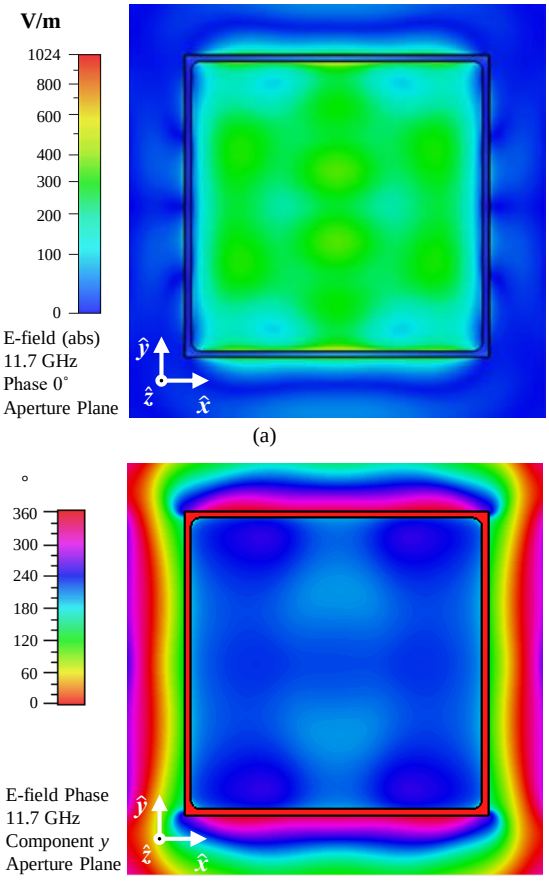

Fig. 10. Simulated distribution of the e-field on the aperture of the AM dual-polarized square aperture Q-FPHA: (a) amplitude and (b) phase.

9(d)] where horn antennas exhibit maximum values of cross-polarization. In the same figures [Figs. 9(a)-(d)], the ideal case is superimposed (solid lines). This is the case of an aperture with the same dimensions (67 mm × 67 mm) illuminated by a totally uniform and unidirectional electric field distribution. After applying the equivalence principle

This article has been accepted for publication in a future issue of this journal, but has not been fully edited. Content may change prior to final publication. Citation information: DOI 10.1109/OJAP.2021.3134833, IEEE Open Journal of Antennas and Propagation

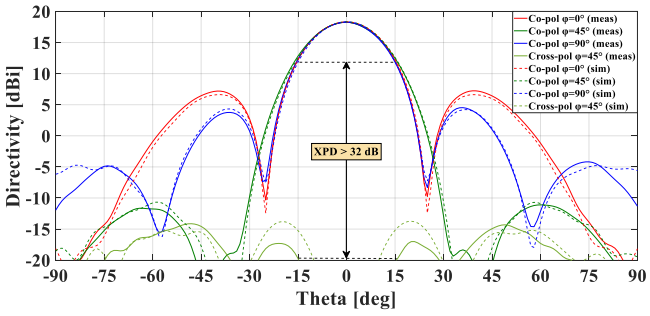

(a)

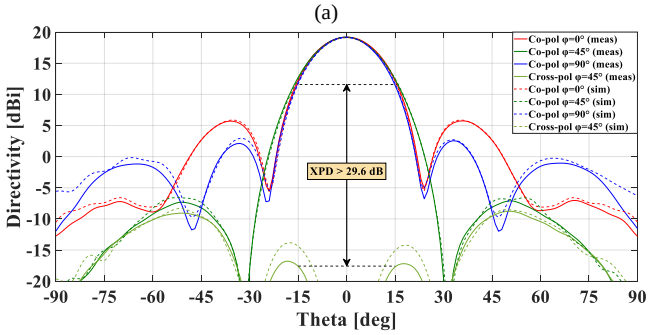

(b)

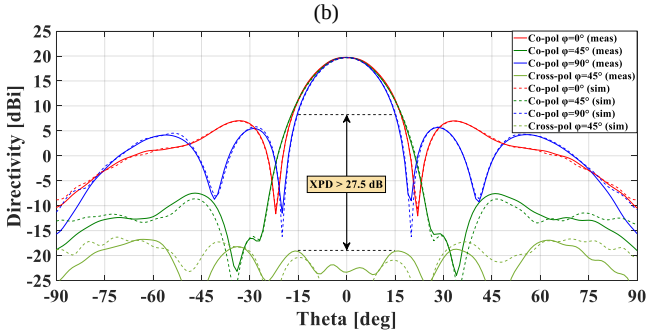

(c)

Fig. 11. Measured (solid lines) and simulated (dashed lines) directivity patterns at: (a) 10.7 GHz, (b) 11.7 GHz and (c) 12.75 GHz.

[1], we obtain the directivity patterns of an identical aperture which produces the maximum far-field directivity radiation pattern (or ideally maximum directivity, i.e. 100%). A very close agreement between the two cases is observed, displaying the excellent radiation performance of the developed antenna. The sidelobe level in the E- and H-planes is close to the value of 13.26 dB below the main lobe peak, which corresponds to a uniform aperture distribution of a square aperture. The worst-case cross-polarization level is 28 dB below the co-polarized peak which denotes a nearly identical E- and H- plane patterns due to an almost uniform aperture excitation. The amplitude and phase of the electric field on the aperture have been calculated with CST and are depicted in Figs. 10(a) and 10(b), respectively.

Figs. 11(a)-(c) illustrate the measured and numerically predicted directivity patterns (the co-polarized pattern is shown for the φ = 0˚, 45˚, 90˚ cuts and the cross-polarized pattern for the φ = 45˚ cut) at the lowest (10.7 GHz), central (11.7 GHz) and highest (12.75 GHz) frequencies of the transmit Ku-band, respectively. An excellent agreement between measured and simulated values is observed. The cross-polarization discrimination (XPD) for the three directivity patterns is also depicted. The XPD is defined as

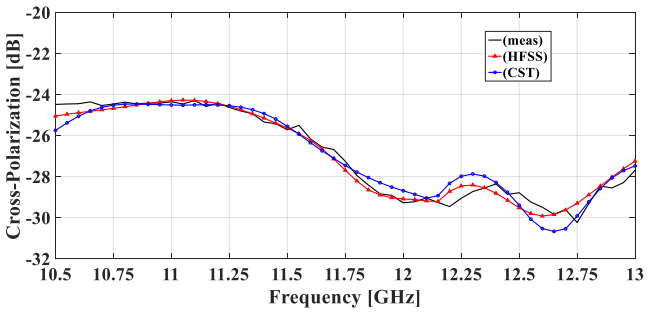

Fig. 12. Measured (solid lines) and simulated (solid dotted lines) cross-polarization of the AM dual-polarized Q-FPHA over a solid angle of ±90˚.

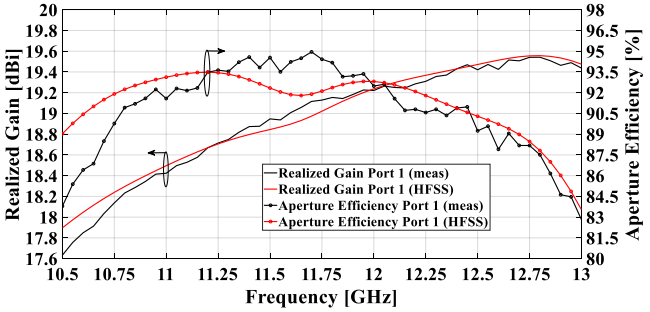

(a)

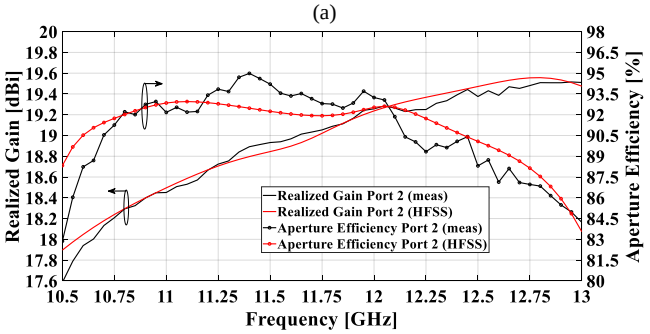

(b)

Fig. 13. Measured and simulated realized gain (solid lines) and aperture efficiency (solid dotted lines) for excitation of: (a) port 1 and (b) port 2.

the ratio of the co-polar component compared to the orthogonal cross-polar component over a specific beamwidth solid angle. In our case, the antenna feed exhibits its minimum XPD (above 27 dB) over a solid angle sector of ±30˚ at the highest frequency of 12.75 GHz. The simulated and measured maximum cross-polarization across the frequency of the AM antenna feed are depicted in Fig. 12. The cross-polarization [or cross-polarized isolation, (XPI)] is the ratio of the maximum co-polar component to the maximum orthogonal cross-polar component over a solid angle of ±90˚. High-efficiency square horns are typically used in array configurations and specifications for cross-polarization call usually for a solid angle range of ±10˚. In other words, what is practically more important, is the cross-polarization performance within the scanning limit [2], [18]. For this range (±10˚), the antenna exhibits experimental maximum XPI values above 35 dB and XPD values above 30 dB, which are excellent levels for almost all applications.

The last subject to be addressed relates to the evaluation of the AM dual-polarized square aperture Q-FPH's losses. Figs. 13(a)-(b) depict the measured and simulated broadside realized gain and aperture efficiency of the AM antenna feed

This article has been accepted for publication in a future issue of this journal, but has not been fully edited. Content may change prior to final publication. Citation information: DOI 10.1109/OJAP.2021.3134833, IEEE Open Journal of Antennas and Propagation

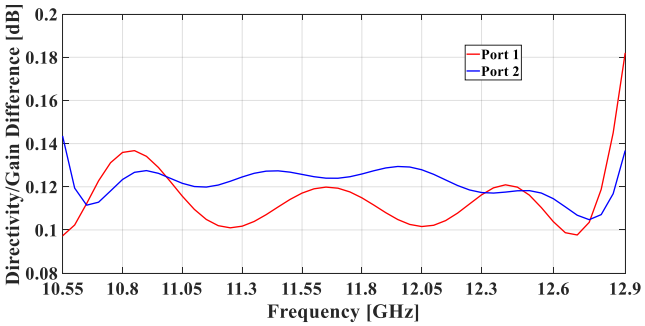

Fig. 14. Numerically estimated losses of the AM dual-polarized Q-FPHA: simulated directivity/realized gain difference curves for both polarizations.

for the excitation of port 1 and 2, respectively. The aperture efficiency has been calculated according to eq. (5) where in this case, the broadside directivity (D_0) is replaced by the broadside realized gain. The aperture flange thickness has not been taken into account in *A*. According to simulations, this thickness results in an average gain increase of around 0.1 dB (around 1.8% in terms of aperture efficiency). The average value of the aperture efficiency is of the order of 91.2% over a fractional bandwidth of 20% (i.e. 10.55-12.9 GHz). The measurements have been performed with the NSI2000 near field measurement system. The realized gain has been measured by post-processing the measured broadside directivity after calibrating using a standard gain horn (SGH) on calculations based on the free space loss between this SGH and the AUT. The uncertainty of the gain measurements as provided by NSI is of the order of ±0.25 dB. This value translates to about ±5% in terms of aperture efficiency. As observed, the worst-case differences between simulated and measured values are of the order of ±0.2 dB (which translates to about ±4% in terms of aperture efficiency). We note that deviations of the order of ±0.2 dB owing to the uncertainty of the gain measurements are commensurate with what is reported in the literature [2], [23], [28]. These discrepancies are also attributed to the standard manufacturing tolerances as well as the uncertainty of the simulation tools and the effective conductivity employed to consider the excessive losses from the surface roughness produced by the printing process.

Fig. 14 depicts the estimated losses of the antenna, as the simulated difference between broadside directivity and realized gain values. In this way the losses of the antenna feed produced due to mismatch (reflection losses) and finite conductivity (ohmic losses) were estimated. The average estimated losses are around 0.12 dB, a level which is in compliance with the experimentally characterized dissipated losses of the excitation network (around 0.1 dB) [53], being the main source of induced losses to the total antenna feed.

Table II includes the state-of-the-art high aperture efficiency radiating elements with square apertures between $2.5\lambda_0 \times 2.5\lambda_0$ and $3\lambda_0 \times 3\lambda_0$. The aperture efficiency of all antennas is calculated by eq. (5) based on the measured (or simulated when not available) broadside directivity. In our case, the aperture's flange contribution has been calculated numerically through simulations and has been de-embedded from the initial measured values so that the comparison can be fair. The aperture efficiency is of the order of the

TABLE II
COMPARISON OF STATE-OF-THE-ART SQUARE APERTURE HIGH EFFICIENCY RADIATING ELEMENTS

Feature \ Ref	[18]	[23]	[25]	[19]	This work
Aperture Size	$3\lambda_0 \times 3\lambda_0$	$3\lambda_0 \times 3\lambda_0$	$2.6\lambda_0 \times 2.6\lambda_0$	$3\lambda_0 \times 3\lambda_0$	$2.6\lambda_0 \times 2.6\lambda_0$
Bandwidth (%)	10	8	18	20	20
Aper. Efficien. (%) [average (%)]	88-90 [≈ 89]	90-93 [≈ 92.3]	80-85 [≈ 82.7]	85-90 [≈ 88.3]	87-95 [≈ 92.5]
Directivity [dBi]	21.5	21.6	18.6	21.5	19
Polarization	Dual	Single	Dual	Dual	Dual
Feeder Included	NO	NO	NO	NO	YES
Profile (λ_0)	7.4	6.4	5	9.8	6.4
Horn Antenna Type	Profiled	Profiled	Profiled	Profiled	Q-FPHA
Results	Simulat.	Experim.	Experim.	Simulat.	Experim.

theoretical limit (93.3%) over a bandwidth larger than 13% (10.7 – 12.2 GHz). The average aperture efficiency is 92.5% over a bandwidth of 20%. It is last noted that the referred directivity values in Table II, relate to the central frequency of the operating bandwidth, where the aperture efficiency is optimal for all references.

The main issues of the profiled single-access horns are the capped aperture efficiency with the bandwidth as well as the height (profile) which is as well associated with the bandwidth. Therefore, for a bandwidth of 10%, profiled horns with aperture efficiency levels around 88-90% present axial profiles (without the OMT) above $7\lambda_0$ [18]. Otherwise, for a double bandwidth (20%), the aperture efficiency level is compromised down to 85%, while the height (without the OMT) is increased up to $9.8\lambda_0$ [19]. As a result, for spline horns with square aperture of the order of $2.6\lambda_0 \times 2.6\lambda_0$, for a bandwidth above 15% and a height (without the OMT) of $5\lambda_0$, a significant compromise with respect to the aperture efficiency (80-85%) is required [25].

V. CONCLUSION

The work presented here validates the methodology and design of an excellent candidate for the next generation GEO satellite communications systems. The Q-FPHA includes the feeding network and achieves a dual-polarization capability, high aperture efficiency, broad bandwidth as well as excellent cross-polarization and port-to-port isolation while still maintaining a light weight and low height profile. The unprecedented aperture efficiency levels demonstrate that the Q-FPHA redefines the state-of-the-art high aperture efficiency antennas used in GEO applications, which relates to the more than 20-years old concept of the single-access profiled horn antennas. The Q-FPHA exhibits average aperture efficiency levels of the order of 92.5% over a 20% fractional bandwidth and therefore provides an average enhancement of about 10 percentage points against flight-qualified profiled square horn antennas used in broadband GEO applications. This corresponds to a gain augmentation of around 0.5 dB. Moreover, the profile of the total antenna feed is relatively compact ($6.4\lambda_0$), as profiled horns with a feeder employed in satellite missions present profiles of at least $7\lambda_0$. Design re-approximations of profiled horns that exhibit aperture efficiency levels around 88% over a 20%

This article has been accepted for publication in a future issue of this journal, but has not been fully edited. Content may change prior to final publication. Citation information: DOI 10.1109/OJAP.2021.3134833, IEEE Open Journal of Antennas and Propagation

fractional bandwidth require a double profile ($10\lambda_0$ without the feeder). This occurs from the fact that by conventional profiling it is hard to control the dispersion of the higher order modes on the aperture over a broad bandwidth. As a result, for broadband operation, the profiled horn's aperture modal content starts to deviate from the ideal case when moving away from the central frequency and therefore the aperture efficiency is degraded. In contrast, the presented methodology based on the quad-furcated profiling provides enhanced stability of the aperture modal content owing to the low dispersion of the quad-furcation's modal transmission coefficients. This results in a more efficient framework to control the aperture modes and hence the aperture efficiency. During the antenna design process, not only was the electromagnetic radiation performance optimized, but the Q-FPHA was also simultaneously engineered to be 3D-printed. Additively manufactured components exhibit lower Passive Intermodulation (PIM) and Electrostatic Discharge (ESD) risk compared to components built in traditional manufacturing (i.e. milling) owing to the nature of the fabrication process to build monolithic bodies. In addition, 3D-printed surfaces also reduce the multipaction risk owing to the increased surface roughness with respect to traditionally machined components [54]-[57]. Therefore, the Q-FPHA was engineered on the whole not only to provide high levels of aperture efficiency but also to cope with the harsh environmental conditions of space as well as to operate in high RF power conditions.

APPENDIX

We derive from Figs. 2(b) and 2(c), the following phase conditions:

$$\left|\varphi_{S^c_{1u,h_{m0}\to h_{10}}} - \varphi_{S^c_{1v,h_{m0}\to h_{10}}}\right| = 0^\circ \Rightarrow e^{j\varphi_{S^c_{1u,h_{m0}\to h_{10}}}} = e^{j\varphi_{S^c_{1v,h_{m0}\to h_{10}}}},\ u=2,4,\ v=3,5\ \&\ m=1,3,5 \tag{A1}$$

$$\left|\varphi_{S^c_{1w,h_{50}\to h_{10}}} - \varphi_{S^c_{1w,h_{m'0}\to h_{10}}}\right| = 180^\circ \Rightarrow e^{j\varphi_{S^c_{1w,h_{50}\to h_{10}}}} = -e^{j\varphi_{S^c_{1w,h_{m'0}\to h_{10}}}},\ w=2,3,4,5\ \&\ m'=1,3 \tag{A2}$$

$$\left|\varphi_{S^c_{1u,h_{m0}\to h_{20}}} - \varphi_{S^c_{1v,h_{m0}\to h_{20}}}\right| = 180^\circ \Rightarrow e^{j\varphi_{S^c_{1u,h_{m0}\to h_{20}}}} = -e^{j\varphi_{S^c_{1v,h_{m0}\to h_{20}}}},\ u=2,4,\ v=3,5\ \&\ m=1,3,5 \tag{A3}$$

$$\left|\varphi_{S^c_{1u,h_{30}\to h_{10}}} - \varphi_{S^c_{1u,h_{30}\to h_{20}}}\right| = 180^\circ \Rightarrow e^{j\varphi_{S^c_{1u,h_{30}\to h_{10}}}} = -e^{j\varphi_{S^c_{1u,h_{30}\to h_{20}}}},\ u=2,4 \tag{A4}$$

$$\left|\varphi_{S^c_{1v,h_{30}\to h_{10}}} - \varphi_{S^c_{1v,h_{30}\to h_{20}}}\right| = 0^\circ \Rightarrow e^{j\varphi_{S^c_{1v,h_{30}\to h_{10}}}} = e^{j\varphi_{S^c_{1v,h_{30}\to h_{20}}}},\ v=3,5 \tag{A5}$$

A comprehensive explanation of (A1)-(A5) follows. Eq. (A1) expresses that all modes of the common waveguide (TE_{10}, TE_{30} and TE_{50}) couple, individually, in phase with the mode TE_{10} of all the excitation waveguides [the solid lines in both Figs. 2(b) and 2(c) present equal phases]. Secondly, the phase coupling between the common mode TE_{50} and the excitation mode TE_{10} is 180° different compared to the phase coupling between the common modes TE_{10} and TE_{30} and the excitation mode TE_{10} for all the excitation waveguides. This condition is expressed in eq. (A2) and is depicted in Figs. 2(b) and 2(c) (the green solid lines are 180° out of phase with respect to the red and blue solid lines). Eq. (A3) states that the mode TE_{20} of the waveguides 2, 4 couples to the common waveguide's modes 180° out of phase with respect to the excitation waveguides 3, 5 [all dashed lines in Fig. 2(b) present a phase shift of 180° in relation to the dashed lines in Fig. 2(c)]. Finally, the coupling phase between the mode TE_{10} of the waveguides *u* and the common aperture mode TE_{30} differs by 180° compared to the coupling phase between the mode TE_{20} for the same waveguides (*u*) and the common aperture mode TE_{30} [the two blue lines in Fig. 2(b) present a phase difference of 180°]. This is expressed in eq. (A4). Conversely, as dictated by eq. (A5), the coupling phase between the mode TE_{10} of the waveguides *v* and the common aperture mode TE_{30} is the same (0°) compared to the coupling phase between the mode TE_{20} for the same waveguides (*v*) and the common aperture mode TE_{30} [the two blue lines in Fig. 2(c) are in phase].

Due to eqs. (A1)-(A5) and (4), eq. (3) is simplified as:

$$\begin{bmatrix} F_1^{h_{10}} \\ F_1^{h_{30}} \\ F_1^{h_{50}} \end{bmatrix} = 2\begin{bmatrix} \left|h_{10}^{\text{in}}\right|\cdot e^{j\varphi_{2,h_{10}^{\text{in}}}}\cdot\left|S^c_{12,h_{10}\to h_{10}}\right| + \left|h_{20}^{\text{in}}\right|\cdot e^{j\varphi_{2,h_{20}^{\text{in}}}}\cdot\left|S^c_{12,h_{10}\to h_{20}}\right| \\ \left|h_{10}^{\text{in}}\right|\cdot e^{j\varphi_{2,h_{10}^{\text{in}}}}\cdot\left|S^c_{12,h_{30}\to h_{10}}\right| - \left|h_{20}^{\text{in}}\right|\cdot e^{j\varphi_{2,h_{20}^{\text{in}}}}\cdot\left|S^c_{12,h_{30}\to h_{20}}\right| \\ -\left|h_{10}^{\text{in}}\right|\cdot e^{j\varphi_{2,h_{10}^{\text{in}}}}\cdot\left|S^c_{12,h_{50}\to h_{10}}\right| - \left|h_{20}^{\text{in}}\right|\cdot e^{j\varphi_{2,h_{20}^{\text{in}}}}\cdot\left|S^c_{12,h_{50}\to h_{20}}\right| \end{bmatrix} \tag{A6}$$

The phase of the excitation mode TE_{20} is expressed as a function of the phase of the first excitation mode TE_{10} as:

$$\varphi_{2,h_{20}^{\text{in}}} = \varphi_{2,h_{10}^{\text{in}}} - \Delta\varphi_{\text{in}} \Rightarrow e^{j\varphi_{2,h_{20}^{\text{in}}}} = e^{j\varphi_{2,h_{10}^{\text{in}}}}\cdot e^{-j\Delta\varphi_{\text{in}}} \tag{A7}$$

so that eq. (A6) can be written as below:

$$\begin{bmatrix} F_1^{h_{10}} \\ F_1^{h_{30}} \\ F_1^{h_{50}} \end{bmatrix} = 2\begin{bmatrix} e^{j\varphi_{2,h_{10}^{\text{in}}}}\cdot\left(\left|h_{10}^{\text{in}}\right|\cdot\left|S^c_{12,h_{10}\to h_{10}}\right| + \left|h_{20}^{\text{in}}\right|\cdot\left|S^c_{12,h_{10}\to h_{20}}\right|\cdot e^{-j\Delta\varphi_{\text{in}}}\right) \\ e^{j\varphi_{2,h_{10}^{\text{in}}}}\cdot\left(\left|h_{10}^{\text{in}}\right|\cdot\left|S^c_{12,h_{30}\to h_{10}}\right| - \left|h_{20}^{\text{in}}\right|\cdot\left|S^c_{12,h_{30}\to h_{20}}\right|\cdot e^{-j\Delta\varphi_{\text{in}}}\right) \\ e^{j\varphi_{2,h_{10}^{\text{in}}}}\cdot\left(-\left|h_{10}^{\text{in}}\right|\cdot\left|S^c_{12,h_{50}\to h_{10}}\right| - \left|h_{20}^{\text{in}}\right|\cdot\left|S^c_{12,h_{50}\to h_{20}}\right|\cdot e^{-j\Delta\varphi_{\text{in}}}\right) \end{bmatrix} \tag{A8}$$

The phase of the excitation mode TE_{10}, $\varphi_{2,h_{10}^{\text{in}}}$, appears in each term of the common waveguide modes $F_1^{h_{m0}}$, m = 1, 3, 5, thus without loss of generality is considered zero and can be eliminated.

This article has been accepted for publication in a future issue of this journal, but has not been fully edited. Content may change prior to final publication. Citation information: DOI 10.1109/OJAP.2021.3134833, IEEE Open Journal of Antennas and Propagation

Last, the total power (normalized to 1) of each excitation waveguide is allocated to these modes as:

$$\left|h_{10}^{\text{in}}\right|=\sqrt{1-\left|h_{20}^{\text{in}}\right|^2} \tag{A9}$$

ACKNOWLEDGMENT

The authors want to thank Thierry Pierré for his advices and support to the mechanical model and the prototyping, as well as Philippe Gatinet for his help with the measurements.

REFERENCES

[1] C. Balanis, *Antenna Theory and Design*. Hoboken, NJ, USA: Wiley, 2015.

[2] L. Shafai, S. K. Sharma, and S. Rao, *Handbook of Reflector Antennas and Feed Systems: Feed Systems* (Artech House Antennas and Propagation Library), vol. 2. Norwood, MA, USA: Artech House, 2013.

[3] J. C. Lafond *et al*., "Thales Alenia Space multiple beam antennas for telecommunication satellites," *Proc. 8th Eur. Conf. Antennas Propag. (EuCAP'14),* pp. 186-190, Apr. 2014.

[4] H. Wolf, and E. Sommer, "An Advanced Compact Radiator Element for Multifeed Antennas," *Proc. 18th Eur. Microw. Conf.*, Stockholm, Sweden, 1988, pp. 506-511.

[5] S. A. Muhammad, A. Rolland, S. H. Dahlan, R. Sauleau, and H. Legay, "Hexagonal-Shaped Broadband Compact Scrimp Horn Antenna for Operation in C-Band," *IEEE Antennas Wireless Propag. Lett.*, vol. 11, pp. 842-845, 2012.

[6] P. Ingvarson, U. Jostell, and P. Svedjenas, "Patch-excited cup elements for satellite-based mobile communication antennas," *Proc. IEEE Int. Conf. Phased Array Syst. Technol.*, pp. 215-218, May 2000.

[7] M. Rayner, A. D. Olver, and A. D. Monk, "FD-TD design of short backfire antennas," *IEE Proc.-Microw. Antennas Propagat.*, vol. 144, no. 1, pp. 1-6, Feb. 1997.

[8] M. G. Bray, and E. Lier, "High Efficiency Short Backfire Antenna Using Electromagnetically Hard Walls," *IEEE Antennas Wireless Propag. Lett.*, vol. 14, pp. 1614-1617, 2015.

[9] J. D. Binion, E. Lier, D. H. Werner, T. H. Hand, Z. H. Jiang, and P. L. Werner, "Metasurface-Enabled Advanced Short Backfire Antenna," *IEEE Trans. Antennas Propag.*, vol. 68, no. 3, pp. 1302-1311, Mar. 2020.

[10] S. A. Muhammad, R. Sauleau, and H. Legay, "Small-Size Shielded Metallic Stacked Fabry–Perot Cavity Antennas With Large Bandwidth for Space Applications," *IEEE Trans. Antennas Propag.*, vol. 60, no. 2, pp. 792-802, Feb. 2012.

[11] M. S. Aly, and S. F. Mahmoud, "Propagation and radiation behaviour of a longitudinally slotted horn with dielectric-filled slots," *Proc. Inst. Elect. Eng.H. Microw. Antennas Propag.*, vol. 132, pp. 477-479, 1985.

[12] A. Rolland, *N. T. Nguyen*, R. Sauleau, Ch. Person, and L. Le Coq, "Smooth-walled light-weight Ka-band shaped horn antennas in metalized foam", *IEEE Trans. Antennas Propag*., vol. 60, no. 3, pp. 1245-1251, Mar. 2012.

[13] A. Rolland, A. Boriskin, Ch. Person, C. Quendo, L. Le Coq, and R. Sauleau, "Lens-corrected axis-symmetrical shaped horn antenna in metalized foam with improved bandwidth", *IEEE Antennas Wireless Propag. Lett.*, vol. 11, pp. 57-60, 2012.

[14] O. Sotoudeh, P.-S. Kildal, P. Ingvarson, and S. P. Skobelev, "Single- and dual-band multimode hard horn antennas with partly corrugated walls," *IEEE Trans. Antennas Propag.*, vol. 54, no. 2, pp. 330-339, Feb. 2006.

[15] E. Lier, D. H. Werner, and T. S. Bird, "The Evolution From Metal Horns to Metahorns: The development of EM horns from their inception to the present day," *IEEE Antennas Propag. Mag.*, vol. 61, no. 4, pp. 6-18, Aug. 2019.

[16] V. Sozio *et al*., "Design and Realization of a Low Cross-Polarization Conical Horn With Thin Metasurface Walls," *IEEE Trans. Antennas Propag*., vol. 68, no. 5, pp. 3477-3486, May 2020.

[17] A. Rolland, M. Ettorre, M. Drissi, L. Le Coq and R. Sauleau, "Optimization of Reduced-Size Smooth-Walled Conical Horns Using BoR-FDTD and Genetic Algorithm," *IEEE Trans. Antennas Propag.*, vol. 58, no. 9, pp. 3094-3100, Sept. 2010.

[18] A. K. Bhattacharyya, and G. Goyette, "A novel horn radiator with high aperture efficiency and low cross-polarization and applications in arrays and multibeam reflector antennas," *IEEE Trans. Antennas Propag*., vol. 52, no. 11, pp. 2850-2859, Nov. 2004.

[19] E. Agastra, G. Bellaveglia, L. Lucci, R. Nesti, G. Pelosi, G. Ruggerini, and S. Selleri, "Genetic Algorithm Optimization of High-Efficiency Wide-Band Multimodal Square Horns for Discrete Lenses," *Prog. Electromagnet. Res.*, Vol. 83, 335-352, 2008.

[20] G. Ruggerini, "A compact circular horn with high efficiency," *Proc. 4th Eur. Conf. Antennas Propag. (EuCAP'10),* pp. 186-190, Apr. 2010.

[21] A. Kumar, and R. Jyoti, "High aperture efficiency profiled horn at Ku-band," *Proc. IEEE Int. Conf. Antenna Innov. Mod. Technol. Ground Aircr. Satell. Appl. (iAIM)*, pp. 1-4, Nov. 2017.

[22] K. K. Chan, and S. K. Rao, "Design of High Efficiency Circular Horn Feeds for Multibeam Reflector Applications," *IEEE Trans. Antennas Propag*., vol. 56, no. 1, pp. 253-258, Jan. 2008.

[23] T. S. Bird, and C. Granet, "Optimization of Profiles of Rectangular Horns for High Efficiency," *IEEE Trans. Antennas Propag.*, vol. 55, no. 9, pp. 2480-2488, Sept. 2007.

[24] I. Albert, M. Romier, D. Belot, J. Adam, and P. Hamel, "Design, manufacturing and test of a spline-profile square horn for focal array applications," *Proc. 15th Int. Symp. Antenna Technol. Appl. Electromagn.*, pp. 1-3, Jun. 2012.

[25] M. Nadarassin *et al*., "PAFSR Reconfigurable Antenna Feed Array Design," *Proc. 15th Int. Symp. Antenna Technol. Appl. Electromagn.*, pp. 1-6, Jun. 2012.

[26] M. Nadarassin *et al*., "Ku-band reconfigurable compact array in dual polarization," *Proc. 5th Eur. Conf. Antennas Propag. (EuCAP'11),* pp. 2857-2861, Apr. 2011.

[27] A. Catalani, L. Russo, O. M. Bucci, T. Isernia, A.F. Morabito, S. Perna, D. Pinchera, and G. Toso, "Sparse arrays for satellite communications: from optimal design to realization", *32nd ESA Antenna Workshop*, Noordwijk, The Netherlands, Oct. 5-10 2010.

[28] C. Stoumpos, J.-P. Fraysse, G. Goussetis, C. G. González, R. Sauleau and H. Legay, "Highly Efficient Broadband Pyramidal Horn with Integrated H-Plane Power Division," *IEEE Trans. Antennas Propag.*, early access, Sep. 15, 2021. doi: 10.1109/TAP.2021.3111276.

[29] J.-P. Fraysse, C. Stoumpos, H. Legay and S. Tubau, "Multiple-Port Radiating Element," US Patent, Pub. No. US 2020/0176878 A1, Jun. 4, 2020.

[30] A. Cherrette, R. Parrikar, and T. Smith, "High Efficiency Dual Polarized Horn Antenna," US Patent, Pub. No. US 2001/6211838 B1, Apr. 2001.

[31] R. Shen, X. Ye and J. Miao, "Design of a Multimode Feed Horn Applied in a Tracking Antenna," *IEEE Trans. Antennas Propag.*, vol. 65, no. 6, pp. 2779-2788, Jun. 2017.

[32] R. E. Collin, *Field Theory of Guided Waves* (IEEE/OUP Series on Electromagnetic Wave Theory). Piscataway, NJ, USA: IEEE Press, 1991.

[33] N. Marcuvitz, *Waveguide Handbook*. N. Y., New York: McGraw-Hill Book Co., Inc., 1951.

[34] L. Polo-López, J. Córcoles, J. A. Ruiz-Cruz, J. R. Montejo-Garai, and J. M. Rebollar, "On the Theoretical Maximum Directivity of a Radiating Aperture From Modal Field Expansions," *IEEE Trans. Antennas Propag.*, vol. 67, no. 4, pp. 2781-2786, Apr. 2019.

[35] S. K. Rao, and C. Ostroot, "Design Principles and Guidelines for Phased Array and Reflector Antennas," *IEEE Antennas Propag. Mag.*, vol. 62, no. 2, pp. 74-81, Apr. 2020.

[36] J. Uher, J. Bornemann, and U. Rosenberg, *Waveguide Components for Antenna Feed Systems: Theory and CAD*. Norwood, MA, USA: Artech House, 1993.

[37] J. M. Rebollar, and J. A. Encinar, "Field theory analysis of multiport-multidiscontinuity structures: An application to short-circuited E-plane septum," *Proc. Inst. Elect. Eng. Microw. Antennas Propag.*, vol. 135, no. 1, pp. 1-7, Feb. 1988.

[38] S. Tubau *et al*., "Design of a Compact Four-Way Dual Polarization Orthomode Power Divider for Multiport Radiating Elements," *Proc. 13th Eur. Conf. Antennas Propag. (EuCAP'19),* pp. 1-5, Mar. 2019.

[39] C. Stoumpos, J.-P. Fraysse, S. Tubau, G. Goussetis, R. Sauleau, and H. Legay, "A Compact and Broadband Four-Way Dual Polarization

Waveguide Power Divider for Antenna Arrays," *Proc. 14th Eur. Conf. Antennas Propag. (EuCAP'20),* pp. 1-5, Mar. 2020.

[40] N. J. G. Fonseca, "Broadband Waveguide Dual-Polarization Four-Way Power Divider for Small Passive Arrays," *IEEE Microw. Wireless Compon. Lett.*, vol. 31, no. 8, pp. 985-988, Aug. 2021.

[41] G. Han, B. Du, W. Wu, and B. Yang, "A Novel Hybrid Phased Array Antenna for Satellite Communication on-the-Move in Ku-band," *IEEE Trans. Antennas Propag.*, vol. 63, no. 4, pp. 1375-1383, Apr. 2015.

[42] J. L. Cano, A. Mediavilla, S. Dragas, and A. Tazón, "Novel Broadband Circular Waveguide Four-Way Power Divider for Dual Polarization Applications," *IEEE Microw. Wireless Compon. Lett.*, vol. 26, no. 2, pp. 98-100, Feb. 2016.

[43] E. Garcia-Marin *et al.*, "Dual Circularly Polarized Array Antenna based on Corporate Feeding Network in Square Waveguide Technology," *IEEE Trans. Antennas Propag.*, vol. 69, no. 3, pp. 1763-1768, March 2021.

[44] A. Morini, M. Baldelli, P. Angeletti, D. Petrolati, G. Toso, and G. Venanzoni, "Directional coupler with 3 input / 3 output square waveguide dual-polarization ports," *Proc. 13th Eur. Conf. Antennas Propag. (EuCAP'18)*, pp. 1-4, Apr. 2018.

[45] E. Menargues *et al*., "Four-Port Broadband Orthomode Transducer Enabling Arbitrary Interelement Spacing," *IEEE Trans. Microw. Theory and Techn.*, vol. 66, no. 12, pp. 5521-5530, Dec. 2018.

[46] N. J. G. Fonseca, and P. Rinous, "Compact orthomode power divider for high-efficiency dual-polarisation rectangular horn antennas," *Proc. 6th Eur. Conf. Antennas Propag. (EuCAP'12)*, pp. 1024-1027, Mar. 2012.

[47] N. J. G. Fonseca, D. Petrolati, and P. Angeletti, "Design of a waveguide dual-mode three-way power divider for dual-polarization beam forming networks at Ka-band," in *Proc. IEEE Antennas Propag. Soc. Int. Symp. (APSURSI)*, Orlando, FL, USA, pp. 1096–1097, Jul. 2013.

[48] D. Kim, M. Zhang, J. Hirokawa, and M. Ando, "Design and Fabrication of a Dual-Polarization Waveguide Slot Array Antenna With High Isolation and High Antenna Efficiency for the 60 GHz band," *IEEE Trans. Antennas Propag.*, vol. 62, no. 6, pp. 3019-3027, Jun. 2014.

[49] J. Wu, Y. J. Cheng, H. B. Wang, Y. C. Zhong, D. Ma, and Y. Fan, "A Wideband Dual Circularly Polarized Full-Corporate Waveguide Array Antenna Fed by Triple-Resonant Cavities," *IEEE Trans. Antennas Propag.*, vol. 65, no. 4, pp. 2135-2139, April 2017.

[50] S. Zhou, G. Huang, T. Chio, J. Yang, and G. Wei, "Design of a Wideband Dual-Polarization Full-Corporate Waveguide Feed Antenna Array," *IEEE Trans. Antennas Propag.*, vol. 63, no. 11, pp. 4775-4782, Nov. 2015.

[51] X. Lu, H. Zhang, S. Gu, H. Liu, X. Wang, and W. Lu, "A Dual-Polarized Cross-Slot Antenna Array on a Parallel-Plate Waveguide With Compact Structure and High Efficiency," *IEEE Antennas Wireless Propag. Lett.*, vol. 17, no. 1, pp. 8-11, 2018.

[52] C. Stoumpos, J.-P. Fraysse, G. Goussetis, R. Sauleau, C. G. González and H. Legay, "Compact and Highly Efficient Single and Dual Polarized Aperture Antennas with Integrated Multiport Overmoded Excitation," *Proc. 15th Eur. Conf. Antennas Propag. (EuCAP'21),* pp. 1-5, Mar. 2021.

[53] C. Stoumpos *et al.*, "Four-Way Orthomode Waveguide Power Dividers: Subtractive and Additive Manufacturing," *Proc. 15th Eur. Conf. Antennas Propag. (EuCAP'21),* pp. 1-5, Mar. 2021.

[54] P. Martin-Iglesias *et al.*, "Enhanced multipactor performance in 3D printed microwave parts," in *Proc. IEEE MTT-S Int. Microw. Workshop Series Adv. Mater. Process. (IMWS-AMP)*, Pavia, Italy, Sep. 2017, pp. 1–3.

[55] D. Wu *et al.*, "Fabrication of porous Ag/TiO2/Au coatings with excellent multipactor suppression", *Sci. Rep.*, vol. 7, Mar. 2017.

[56] V. Nistor *et al.*, "Multipactor suppression by micro-structured gold/silver coatings for space applications", *Appl. Surf. Sci.*, vol. 315, pp. 445-453, Oct. 2014.

[57] C. Stoumpos, M. García-Vigueras, J. -A. Duran-Venegas and T. Pierré, "Additively Manufactured High Power Microwave Components in Aluminum SLM*," *Proc. IEEE ICOPS*, pp. 1-1, Sep. 2021. doi: 10.1109/ICOPS36761.2021.9588609

Stoumpos Charalampos was born in Thessaloniki, Greece, in 1990. He received the Diploma and M.Sc. degrees (Hons.) in electrical and computer engineering from the Democritus University of Thrace, Xanthi, Greece, in 2015 and 2017, respectively, and the Ph.D. degree from the Heriot-Watt University, Edinburgh, U.K, in 2020. Since February 2021 he is a post-doc in INSA Rennes, Rennes, France. His PhD was part of the European Union's Horizon 2020 research and innovation program under the Marie Skłodowska-Curie Grant Agreement REVOLVE in partnership with Thales Alenia Space, Toulouse, France, where he spent two years as a Research Fellow in the Department of Research and Technology. His current research interests include microwave components, high aperture efficiency antennas, frequency selective surfaces and additive manufacturing.

Jean-Philippe Fraysse received the Ph.D. degree from the University of Limoges, Limoges, France, in 1999. In 1999, he joined Thales Alenia Space, Toulouse, France, where he is currently a Microwave Research Engineer. His current research interests include active satellite antennas, MMICs, power amplifiers and high frequency microwave components.

George Goussetis (Senior Member, IEEE) received the Diploma degree in electrical and computer engineering from the National Technical University of Athens, Greece, in 1998, the B.Sc. degree in physics (Hons.) from University College London, U.K., in 2002, and the Ph.D. degree from the University of Westminster, London, U.K., in 2002. In 1998, he joined Space Engineering, Rome, Italy, as an RF Engineer, and as a Research Assistant with the Wireless Communications Research Group, University of Westminster, U.K., in 1999. From 2002 to 2006, he was a Senior Research Fellow with Loughborough University, U.K. He was a Lecturer (Assistant Professor) with Heriot-Watt University, Edinburgh, U.K., from 2006 to 2009, and a Reader (Associate Professor) with Queen's University Belfast, U.K., from 2009 to 2013. In 2013, he joined Heriot-Watt, as a Reader, and was promoted to Professor, in 2014.

He has authored or co-authored over 200 peer-reviewed papers five book chapters one book and two patents. His research interests include the modelling and design of microwave filters, frequency-selective surfaces and periodic structures, leaky wave antennas, microwave sensing and curing as well numerical techniques for electromagnetics. Dr. Goussetis has held a research fellowship with the Onassis Foundation in 2001, a research fellowship with the U.K. Royal Academy of Engineering from 2006 to 2011, and a European Marie-Curie experienced researcher fellowship from 2011 to 2012. He was a co-recipient of the 2011 European Space Agency Young Engineer of the Year Prize, the 2011 EuCAP Best Student Paper Prize, the 2012 EuCAP Best Antenna Theory Paper Prize, and the 2016 Bell Labs Prize.

This article has been accepted for publication in a future issue of this journal, but has not been fully edited. Content may change prior to final publication. Citation information: DOI 10.1109/OJAP.2021.3134833, IEEE Open Journal of Antennas and Propagation

Ronan Sauleau (M'04–SM'06–F'18) graduated in electrical engineering and radio communications from the Institut National des Sciences Appliquées, Rennes, France, in 1995. He received the Agrégation degree from the Ecole Normale Supérieure de Cachan, France, in 1996, and the Doctoral degree in signal processing and telecommunications and the "Habilitation à Diriger des Recherches" degree, both from the University of Rennes 1, France, in 1999 and 2005, respectively.

He was an Assistant Professor and Associate Professor at the University of Rennes 1, between September 2000 and November 2005, and between December 2005 and October 2009, respectively. He has been appointed as a full Professor in the same University since November 2009. His current research fields are numerical modeling (mainly FDTD), millimeter-wave printed and reconfigurable (MEMS) antennas, substrate integrated waveguide antennas, lens-based focusing devices, periodic and non-periodic structures (electromagnetic bandgap materials, metamaterials, reflectarrays, and transmitarrays) and biological effects of millimeter waves. He has been involved in more than 60 research projects at the national and European levels and has co-supervised 23 post-doctoral fellows, 44 PhD students and 50 master students.

He has received 17 patents and is the author or coauthor of more than 260 journal papers and 510 publications in international conferences and workshops. He has shared the responsibility of the research activities on antennas at IETR in 2010 and 2011. He was co-director of the research Department 'Antenna and Microwave Devices' at IETR and deputy director of IETR between 2012 and 2016. He is now director of IETR. Prof. Sauleau received the 2004 ISAP Conference Young Researcher Scientist Fellowship (Japan) and the first Young Researcher Prize in Brittany, France, in 2001 for his research work on gain-enhanced Fabry-Perot antennas. In September 2007, he was elevated to Junior member of the "Institut Universitaire de France". He was awarded the Bronze medal by CNRS in 2008, and the silver medal in 2020. He was the co-recipient of several international conference awards with some of his students (Int. Sch. of BioEM 2005, BEMS'2006, MRRS'2008, E-MRS'2011, BEMS'2011, IMS'2012, Antem' 2012, BioEM'2015, EuCAP'2019). He served as a guest editor for the IEEE Antennas Propogat. Special Issue on "Antennas and Propagation at mm and sub mm waves". He served as a national delegate for several EU COST actions. He has served as a national delegate for EurAAP and as a member of the board of Director of EurAAP from 2013 to 2018.

Hervé Legay received the electrical engineering and Ph.D. degrees from the National Institute of Applied Sciences, Rennes, France, in 1988 and 1991, respectively. He was then a Post-Doctoral Fellow with the University of Manitoba, Winnipeg, MB, Canada.

In 1994, he joined Alcatel Space (now Thales Alenia Space), Toulouse, France. He initially conducted studies in the areas of military telecommunication satellite antennas and antenna processing. He designed the architecture and the antijamming process of the Syracuse 3 active antenna. He is currently the Head of the R&T on space antennas, developing new antenna concepts with emerging technologies (Reflectarrays, integrated antennas, multiple beam quasi-optical antennas, innovative active architectures, antenna processing, …). He is co-Director of the joint laboratory MERLIN, involving Thales Alenia Space, and the Institut d'Electronique et de Télécommunication de Rennes. Dr. Legay is the Chair of a group of Antenna Experts in Thales Group. He coordinates the collaborations with academic and research partners. He has authored 35 patents. He was a co-prize winner of the 2007 Schelkunoff Prize Paper Award. He was a recipient of the Gold Thales Awards in 2008, a reward for the best innovations in the Thales Group.